Diffraction phase microscopy with white light

Basanta Bhaduri, Hoa Pham, Mustafa Mir, and Gabriel Popescu*

Quantitative Light Imaging Laboratory, Department of Electrical and Computer Engineering, Beckman Institute for Advanced Science and Technology, University of Illinois at Urbana-Champaign, Urbana, Illinois 61801, USA
**Corresponding author: gpopescu@illinois.edu*

Received December 13, 2011; revised January 24, 2012; accepted January 24, 2012;
posted January 25, 2012 (Doc. ID 159922); published March 14, 2012

We present white light diffraction phase microscopy (wDPM) as a quantitative phase imaging method that combines the single shot measurement benefit associated with off-axis methods, high temporal phase stability associated with common path geometries, and high spatial phase sensitivity due to the white light illumination. We propose a spatiotemporal filtering method that pushes the limit of the pathlength sensitivity to the subangstrom level at practical spatial and temporal bandwidths. We illustrate the utility of wDPM with measurements on red blood cell morphology and HeLa cell growth over 18 hours. © 2012 Optical Society of America

OCIS codes: 170.0180, 120.5050, 070.6110, 050.1950.

Quantitative phase imaging (QPI) is an emerging field developing at an accelerating pace over the past several years [1]. In QPI, we measure the optical pathlength map associated with transparent specimens and translate this data into biomedically relevant information. The main figures of merit in QPI are (1) acquisition rate, (2) transverse resolution, (3) temporal phase sensitivity, and (4) spatial phase sensitivity (see Chapter 8 in [1]). The fastest acquisition rates are allowed by off-axis methods, because the phase information is extracted from a single recorded interferogram [2,3]. The diffraction limited transverse resolution is intrinsically preserved in phase shifting methods (for example, off-axis techniques may degrade transverse resolution) [4,5]. The highest temporal phase sensitivity (that is, smallest frame-to-frame phase shift) is provided by common-path methods because they are the most stable [6,7]. Finally, the highest spatial phase sensitivity (i.e., smallest point-to-point phase change within the same frame) is obtained in the absence of speckles [8–11].

Diffraction phase microscopy (DPM) is both off-axis and common-path such that it combines both the benefits of fast acquisition rates and high temporal sensitivity [7,12]. These features enabled DPM to perform unprecedented biological studies, especially related to red blood cell membrane dynamics [13–16]. However, due to the laser illumination, DPM images suffer from speckles, which ultimately degrade the spatial phase sensitivity and limit the applicability for studying subcellular structures. Spatial light interference microscopy (SLIM) removed this obstacle by using white light illumination in a phased shifting geometry [8,11,17,18]. However because of the phase shifting, SLIM requires the acquisition of 4 intensity images for each quantitative phase image.

Here we present white-light DPM (wDPM), which enables single shot images with high spatial and temporal sensitivity. wDPM is implemented as an add-on module to a commercial microscope (Axio Observer Z1, Zeiss). This setup does not require specialized phase contrast optics compared with instantaneous spatial light interference microscopy (iSLIM) [10]. Figure 1 shows the experimental setup, where we employ spatially coherent white light illumination, obtained from a halogen lamp commonly used in commercial microscopes. We close the condenser aperture to the minimum possible value, NA = 0.09, such that the field is spatially coherent over the entire field of view. Illumination power at the sample plane for this NA is 0.16 mW, and for a fully open condenser (NA = 0.55), it is 5.57 mW. As in DPM, at the image plane of the inverted microscope, we place an amplitude diffraction grating that generates multiple diffraction orders containing full spatial information about the object. The zeroth- and first-order beams are isolated at the Fourier plane generated by lens L_1 using a spatial light modulator (SLM) as shown in Fig. 1. The zeroth-order beam is spatially low-pass filtered so that only the DC component of the zeroth order is passed, whereas the first order is completely passed. The diameter of the pinhole (zeroth-order mask) at the Fourier plane is 200 μm, and the rectangular opening (first-order mask) has a size of 5×2 mm^2. The lens system L_1-L_2 forms a highly stable Mach–Zehnder interferometer. The first order is thus the imaging field, and the zeroth order plays the role of the reference field. Both beams are interfered and generate a spatially modulated interference image, which is then captured by a CCD camera (Hamamatsu ORCA Flash) at the image plane. The common-path geometry matches the optical pathlengths for the sample and reference arms such that the alignment is independent of the wavelength and temporal coherence of the illumination source. The spatially resolved quantitative phase image associated with the sample is retrieved from a single CCD recording via a spatial Hilbert transform, as described in [3]. We assume the live cells as phase objects, which is a common assumption in the field. This is a valid

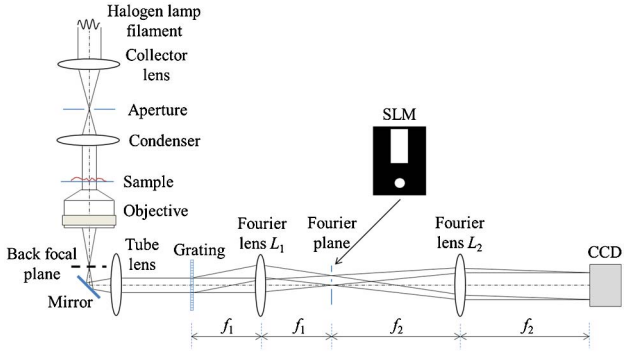

Fig. 1. (Color online) Experimental setup.

approximation as, for unstained cells, bright field images show little to no contrast in intensity. The grating period (9 μm in the present case) was set to be smaller than the diffraction-limited spot of the microscopic imaging system at the grating plane. All the lenses are achromatic to minimize chromatic dispersion. Throughout our experiments, the microscope was equipped with a bright-field 40× (0.75 NA) objective. The L_1-L_2 lens system gives an additional magnification of $f_2/f_1 = 2.5$ so that the sinusoidal modulation of the image is sampled by 6 CCD pixels per period.

In order to characterize the noise stability of our setup, we measured the phase of a time-series of 256 background images of size 512×512 (or 18.5×18.5 μm^2), $\varphi(x, y, t)$, and the phase of a single background image, $\varphi_0(x, y)$, of the same size at a different spatial position. This background phase subtraction allows us to correct for any wavefront curvature, which is a constant associated with our instrument. The spatiotemporal phase noise distribution is then calculated as:

$$\delta\varphi(x, y, t) = \varphi(x, y, t) - \varphi_0(x, y). \quad (1)$$

Figure 2(a) shows such a noise distribution at a particular time. Figure 2(b) describes the noise histogram considering the entire recording time, i.e., the histogram of all $\delta\varphi$ values. This histogram has a standard deviation of $\sigma = 1.1$ nm, which represents the overall spatiotemporal noise of the system, which is approximately an order of magnitude lower than that obtained with DPM (see, e.g., Figs. 3(d) and 3(e) in [8]).

A more complete characterization of the spatiotemporal noise is obtained by numerically computing the spatial and temporal power spectrum as follows (see Chapter 8 in [1]):

$$\phi(\mathbf{k}, \omega) = \alpha \left| \iint_A \int_{-\infty}^{\infty} \delta\varphi(\mathbf{r}, t) \mathbf{e}^{-i(\omega t - \mathbf{k}\cdot\mathbf{r})} \mathrm{d}t \mathrm{d}^2\mathbf{r} \right|^2, \quad (2)$$

where α is a normalization factor such that the area under $\phi(\mathbf{k}, \omega)$ gives the variance of the spatiotemporal noise. This power spectral density describes the contribution to the variance of each temporal and spatial frequency component. Figures 2(c) and 2(d) illustrate this power spectral density along ω and k_x for $k_y = 0$ [Fig. 2(c)] and $k_y = 2\pi$ [Fig. 2(d)], respectively. Our analysis underscores an important capability: by spatial and temporal bandpass filtering, the measurement noise can be reduced significantly. For example, measuring in the frequency range indicated by rectangles A and B in Figs. 2(c) and 2(d) gives an optical pathlength noise level of 0.11 nm and 0.07 nm, respectively. These remarkably low values are obtained for a spatial bandwidth of π rad/μm (0.5 μm spatial distance) in both directions and a temporal bandwidth of 1 rad/s, which are easily achievable in practice. Thus, pathlength changes of sub-angstrom scale can be measured by spatial and temporal filtering. It should be noted that the spatiotemporal filtering is in essence an averaging procedure, and therefore, wDPM's high acquisition rate can be traded for increased sensitivity. The spatial and temporal sensitivities based on spatiotemporal filtering for wDPM are comparable with the values for SLIM (0.3 nm spatially and 0.03 nm temporally [8]).

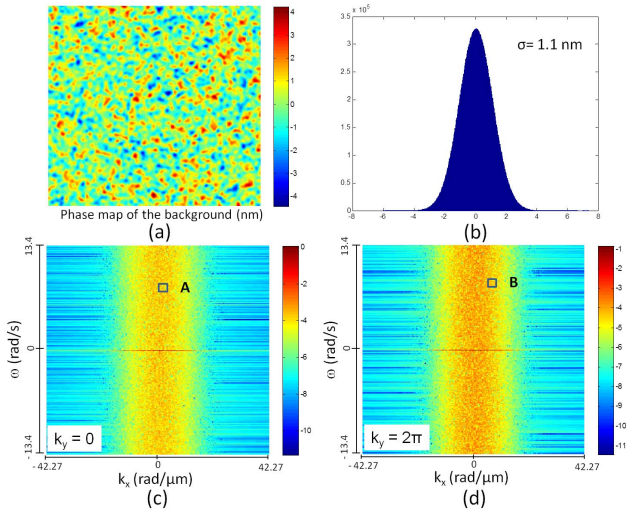

Fig. 2. (Color online) Spatiotemporal noise stability of wDPM. (a) Spatial pathlength noise distribution in a single frame. (b) Spatiotemporal pathlength noise histogram in nanometers. (c) Spatiotemporal power spectral density in log scale at $k_y = 0$. (d) Spatiotemporal power spectral density in log scale at $k_y = 2\pi$. Color bar represents spatiotemporal spectrum of the pathlength in nm^2/[(rad/s)(rad/μm)^2].

To demonstrate the accuracy of the reconstructed phase, we imaged a 2.9 ± 0.14 μm polystyrene bead immersed in immersion oil (Zeiss). Figure 3(a) shows such a phase image. The measured phase value is 2.63 rad, which compares very well with the expected 2.59 ± 0.12 rad at 550 nm (center wavelength of the source). Note that using a low condenser NA reduces the overall illumination power and, accordingly, the frame rate. However, using a sensitive camera, we can currently image at 10 frames/s. Furthermore, by using a higher brightness source (e.g., Mercury HBO, X-Cite), this acquisition rate can be boosted by an order of magnitude.

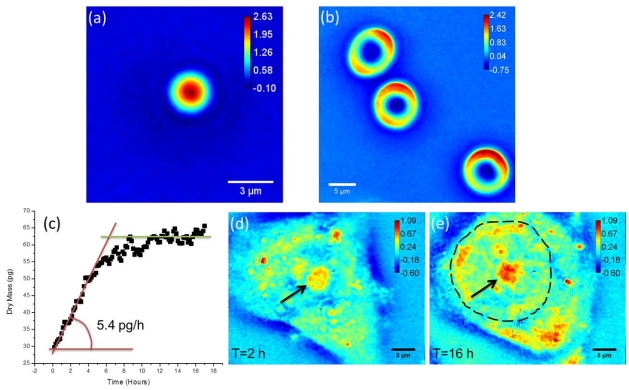

Fig. 3. (Color online) Reconstructed phase image of (a) wDPM image of a polystyrene micro-bead of diameter 2.9 μm. (b) Live red blood cells. (c) Variation of dry mass with time for an isolated HeLa cell during its growth. (d) Time lapse quantitative phase images of the same HeLa cell at $T = 2$ hours. (e) Time lapse quantitative phase images of the same HeLa cell at $T = 16$ hours. Color bars represent phase in radians and arrows point to nucleoli.

Next we imaged live red blood cells (RBC). Prior to imaging, the whole blood was diluted with Coulter LH series diluent (Beckman–Coulter) to a concentration of 0.2% whole blood in solution. Figure 3(b) shows a quantitative phase image of live blood cells, where the normal, discocyte shape can be observed; the color bar shows the phase values in radians. Note that the phase background outside the RBC is much more uniform than in the case of laser illumination.

Furthermore, the wDPM technique is well suited for quantitative measurement of the dry mass, or nonaqueous content, of a living cell. The refractive index of a cell exhibits a strong linear dependence on the total cell protein concentration [19,20]:

$$n(x,y) = n_0 + \eta C(x,y), \tag{3}$$

where η is the refraction increment (in ml/g) and C is the concentration of dry protein in the solution (in g/ml). Using this relationship, the dry mass surface density (ρ) of the cellular matter can be obtained from the measured phase map, φ, as follows:

$$\rho(x,y) = \frac{\lambda}{2\pi\eta}\varphi(x,y), \tag{4}$$

where λ is the center wavelength $\eta = 0.2$ ml/g, which corresponds to an average of reported values [19]. The total dry mass of a cell can then be found by integrating ρ over the entire area of the isolated cell and can be used to quantify cell growth noninvasively [21].

We used a human cervical epithelial cell line, HeLa cells (ATCC, CCL-2), to quantify cell growth. The cells were plated onto a glass bottom dish (MatTek, P35G-1.0-14-C, uncoated) and allowed to settle for 24 hours before imaging. The dish was kept at 37 °C with an incubator XL S1 W/CO2 kit (Zeiss) and a heating insert P S1/Scan stage (Zeiss). Time-lapse wDPM images were acquired once every 10 minutes for 18 hours. The exposure time was 200 ms for each image at 3,200 K, and the transmission shutter was closed before and after each scan. The dish was covered with a cover glass to reduce the effect of evaporation. Figure 3(c) shows the variation of total dry mass in picogram (pg) with time in hours, which clearly reveals the cell growth. This particular cell appears to be growing at a fast rate of 5.4 pg/h for the first 6 hours, after which the growth slows and finally saturates slightly above the double mass level. Higher fluctuations in dry mass at later time points ($T > 6$ hours) are due to cell fragments and debris floating in the culture medium, which adds noise to our measurement. Figures 3(d) and 3(e) show quantitative phase images of the same cell at $T = 2$ hours and $T = 16$ hours, respectively, which reveals the cell structure (nucleolus is indicated by arrow and nucleus is indicated by dashed circle). The negative phase values around the cell are likely due to imperfections in the spatial filter. The SLM filter is obtained from an Epson Powerlite S5 projector with a contrast ratio of 400∶1, which may allow a small portion of the high frequency components to pass.

In summary, wDPM combines the benefits of temporal sensitivity associated with DPM and the spatial sensitivity associated with white light illumination. We have also proposed spatiotemporal frequency bandpass filtering as a means to push the pathlength sensitivity toward the picometer scale at realistic bandwidths.

We are grateful to S. Sridharan for maintaining the HeLa culture. This research was supported by the National Science Foundation (grants CBET 08-46660 CAREER, CBET-1040462 MRI). For more information, visit http://light.ece.uiuc.edu/.

References

1. G. Popescu, *Quantitative Phase Imaging of Cells and Tissues* (McGraw-Hill, 2011).
2. C. Depeursinge, in *Digital Holography and Three-Dimensional Display*, T.-C. Poon, ed. (Springer, 2006), p. 98.
3. T. Ikeda, G. Popescu, R. R. Dasari, and M. S. Feld, Opt. Lett. **30**, 1165 (2005).
4. D. Zicha and G. A. Dunn, J. Microsc. **179**, 11 (1995).
5. W. C. Warger, II and C. A. DiMarzio, Opt. Express **17**, 2400 (2009).
6. G. Popescu, L. P. Deflores, J. C. Vaughan, K. Badizadegan, H. Iwai, R. R. Dasari, and M. S. Feld, Opt. Lett. **29**, 2503 (2004).
7. G. Popescu, T. Ikeda, R. R. Dasari, and M. S. Feld, Opt. Lett. **31**, 775 (2006).
8. Z. Wang, L. J. Millet, M. Mir, H. Ding, S. Unarunotai, J. A. Rogers, M. U. Gillette, and G. Popescu, Opt. Express **19**, 1016 (2011).
9. A. Barty, K. A. Nugent, D. Paganin, and A. Roberts, Opt. Lett. **23**, 817 (1998).
10. H. F. Ding and G. Popescu, Opt. Express **18**, 1569 (2010).
11. Z. Wang, D. L. Marks, P. S. Carney, L. J. Millet, M. U. Gillette, A. Mihi, P. V. Braun, Z. Shen, S. G. Prasanth, and G. Popescu, Opt. Express **19**, 19907 (2011).
12. Y. K. Park, G. Popescu, K. Badizadegan, R. R. Dasari, and M. S. Feld, Opt. Express **14**, 8263 (2006).
13. Y. K. Park, C. A. Best, K. Badizadegan, R. R. Dasari, M. S. Feld, T. Kuriabova, M. L. Henle, A. J. Levine, and G. Popescu, Proc. Natl. Acad. Sci. USA **107**, 6731 (2010).
14. Y. K. Park, C. A. Best, T. Auth, N. Gov, S. A. Safran, G. Popescu, S. Suresh, and M. S. Feld, Proc. Natl. Acad. Sci. USA **107**, 1289 (2010).
15. Y. K. Park, M. Diez-Silva, G. Popescu, G. Lykotrafitis, W. Choi, M. S. Feld, and S. Suresh, Proc Natl. Acad. Sci. USA **105**, 13730 (2008).
16. H. Ding, Z. Wang, F. Nguyen, S. A. Boppart, and G. Popescu, Phys. Rev. Lett. **101**, 238102 (2008).
17. Z. Wang and G. Popescu, Appl. Phys. Lett. **96**, 051117 (2010).
18. Z. Wang, I. S. Chun, X. L. Li, Z. Y. Ong, E. Pop, L. Millet, M. Gillette, and G. Popescu, Opt. Lett. **35**, 208 (2010).
19. R. Barer, Nature **169**, 366 (1952).
20. H. G. Davies and M. H. Wilkins, Nature **169**, 541 (1952).
21. M. Mir, Z. Wang, Z. Shen, M. Bednarz, R. Bashir, I. Golding, S. G. Prasanth, and G. Popescu, Proc. Natl. Acad. Sci. USA **108**, 13124 (2011).